

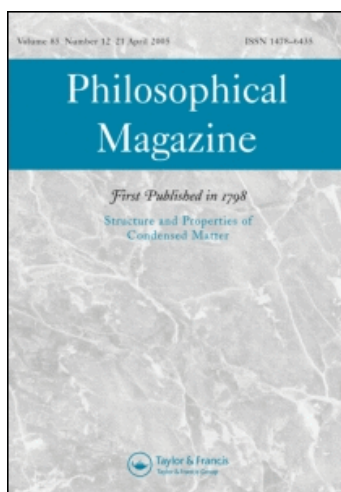
This article was downloaded by: [Koh, A. L.]

On: 17 December 2008

Access details: *Access Details: [subscription number 906939269]*

Publisher *Taylor & Francis*

Informa Ltd Registered in England and Wales Registered Number: 1072954 Registered office: Mortimer House, 37-41 Mortimer Street, London W1T 3JH, UK



## Philosophical Magazine

Publication details, including instructions for authors and subscription information:

<http://www.informaworld.com/smpp/title~content=t713695589>

### Preparation, structural and magnetic characterization of synthetic anti-ferromagnetic (SAF) nanoparticles

A. L. Koh <sup>ab</sup>; W. Hu <sup>a</sup>; R. J. Wilson <sup>a</sup>; S. X. Wang <sup>ac</sup>; R. Sinclair <sup>a</sup>

<sup>a</sup> Department of Materials Science and Engineering, Stanford University, Stanford, USA <sup>b</sup> Department of Mechanical Engineering, Stanford University, Stanford, USA <sup>c</sup> Department of Electrical Engineering, Stanford University, Stanford, USA

Online Publication Date: 01 December 2008

**To cite this Article** Koh, A. L., Hu, W., Wilson, R. J., Wang, S. X. and Sinclair, R. (2008) 'Preparation, structural and magnetic characterization of synthetic anti-ferromagnetic (SAF) nanoparticles', *Philosophical Magazine*, 88:36, 4225 — 4241

**To link to this Article:** DOI: 10.1080/14786430802585133

**URL:** <http://dx.doi.org/10.1080/14786430802585133>

PLEASE SCROLL DOWN FOR ARTICLE

Full terms and conditions of use: <http://www.informaworld.com/terms-and-conditions-of-access.pdf>

This article may be used for research, teaching and private study purposes. Any substantial or systematic reproduction, re-distribution, re-selling, loan or sub-licensing, systematic supply or distribution in any form to anyone is expressly forbidden.

The publisher does not give any warranty express or implied or make any representation that the contents will be complete or accurate or up to date. The accuracy of any instructions, formulae and drug doses should be independently verified with primary sources. The publisher shall not be liable for any loss, actions, claims, proceedings, demand or costs or damages whatsoever or howsoever caused arising directly or indirectly in connection with or arising out of the use of this material.

## Preparation, structural and magnetic characterization of synthetic anti-ferromagnetic (SAF) nanoparticles

A.L. Koh<sup>ab\*</sup>, W. Hu<sup>a</sup>, R.J. Wilson<sup>a</sup>, S.X. Wang<sup>ac</sup> and R. Sinclair<sup>a</sup>

<sup>a</sup>*Department of Materials Science and Engineering, Stanford University, Stanford, USA;*

<sup>b</sup>*Department of Mechanical Engineering, Stanford University, Stanford, USA;* <sup>c</sup>*Department of Electrical Engineering, Stanford University, Stanford, USA*

*(Received 4 June 2008; final version received 27 October 2008)*

Synthetic anti-ferromagnetic nanoparticles (SAFs) are a novel type of magnetic nanoparticle (MNP) fabricated using nanoimprint lithography, direct deposition of multilayer films and retrieval in liquid phase via an ‘etching’ release process. Such physical fabrication techniques enable accurate control of particle shape, size and composition. We systematically varied the processing conditions to produce different configurations of SAF nanoparticles and performed extensive characterization using transmission electron microscopy (TEM) and alternating gradient magnetometry (AGM) to study their corresponding structural and magnetic behavior. A key focus of this paper is the preparation of TEM cross-section specimens of SAF nanoparticles for their structural characterization. This is not a trivial task, but is useful and revealing in terms of structural features. A major finding from our study shows that the introduction of oxygen during deposition of the copper release layer gives significantly improved flatness of the multilayer structure but no significant change in the magnetic properties. Magnetic measurements show that these nanoparticles have nearly zero magnetic remanence, a linear response of magnetization and more than twice the saturation magnetization compared to iron oxide nanoparticles.

**Keywords:** magnetic nanoparticles; magnetic multilayer thin films; transmission electron microscopy; alternating gradient magnetometry

### 1. Introduction

Magnetic nanoparticles (MNPs) are playing increasingly prominent roles in biology and medicine [1–5]. One potential application area is in cell labelling and magnetic separation [6], which is a two-step process involving (i) labelling the target entity with MNPs and then (ii) separating out these tagged entities via a fluid-based magnetic separation mechanism. Such biomedical applications impose several requirements on the MNPs. Structurally, they should be uniform in shape, size and composition [7]. In general, size uniformity is defined by ‘monodispersity’. Particles are considered to be monodisperse in size if the variation is <10%. For good magnetic signals, the MNPs should possess high magnetic moment at low applied magnetic field and low or zero remanence when no magnetic field is applied. The magnetic moment per nanoparticle should also be uniform.

---

\*Corresponding author. Email: [alkoh@stanford.edu](mailto:alkoh@stanford.edu)

The vast majority of these MNPs are synthesized using ‘bottom-up’ chemical methods [8,9] where reagents are injected into hot surfactant solutions to induce the simultaneous formation of many nuclei. The control of particle dimensions is achieved through appropriate manipulation of factors such as choice of surfactants, their ratios with reagent chemicals, reaction rates and temperature. However, there are several limitations in MNPs produced using such techniques. First of all, their dimensions tend to be log-normally distributed with large variations in diameter [10]. Secondly, their sizes need to be constrained to <20 nm in diameter ( $\sim 12$  nm for Fe) [11] because it is only at this length scale that they possess low remanence at zero applied magnetic field (This effect is known as superparamagnetism, whereby the energy which causes the particle magnetic moment to fluctuate is comparable to the thermal energy, and the resulting fluctuations in the direction of magnetization cause the net magnetic moment to average to zero). Owing to their small volumes, the resulting magnetic moments of nanoparticles synthesized using chemical methods tend to be low. One option to enhance the magnetic moment is to create magnetic ‘beads’, where each bead is composed of multiple magnetic cores encapsulated by a (polymer) shell. These beads are already available commercially but studies found that they have the tendency to aggregate [10]. Moreover, the magnetic moment per bead is not uniform due to differences in number of particles per bead.

Recently, a new methodology for fabricating MNPs [12,13] has been developed. This ‘top-down’ approach capitalizes on the formation of patterned templates using nanoimprinting [14–16], direct deposition of material on the templated holes to form nanoparticles and their collection in liquid phase through a release process. Using this technique, high magnetic moment multilayer-structured MNPs – termed synthetic anti-ferromagnetic (SAF) nanoparticles – were made for the first time [13,17,18]. The essential feature of this method involves fabricating the particles to contain two ferromagnetic  $\text{Co}_{90}\text{Fe}_{10}$  layers separated by a nonmagnetic metallic ruthenium (Ru) spacer layer of approximately 2.5 nm (Figure 1a for schematic structure of an SAF nanoparticle). Tantalum (Ta) is used as a capping layer to passivate the surfaces, resulting in excellent chemical stability in solution.

The nomenclature of ‘synthetic anti-ferromagnetics’ [19–21] is standard in the field of magnetic recording (see [22,23], for examples) and refers to the anti-parallel alignment of ferromagnetic layers – usually induced by inter-layer anti-ferromagnetic exchange interactions. However, this effect is induced by both the demagnetizing fields and the anti-ferromagnetic exchange coupling mediated by the Ru spacers. At a spacer thickness of 2.5 nm, the ferromagnetic layers become weakly exchange-coupled and interact primarily through magnetostatic interactions, with like poles repelling. Hence, the magnetizations of the individual layers are anti-parallel at low fields and their moments cancel one another [13].

Since the use of nanoimprint lithography techniques for particle fabrication deviates significantly from conventional chemical synthesis methods, it was postulated that the parameters affecting the structural and magnetic properties of the SAFs will be affected by different parameters compared to MNPs synthesized by wet chemistry. We, therefore, systematically varied processing conditions to produce SAF nanoparticles of different configurations, and performed extensive characterization using transmission electron microscopy (TEM) and alternating gradient magnetometry (AGM) to study their structural and magnetic behavior. This paper describes the findings of our study.

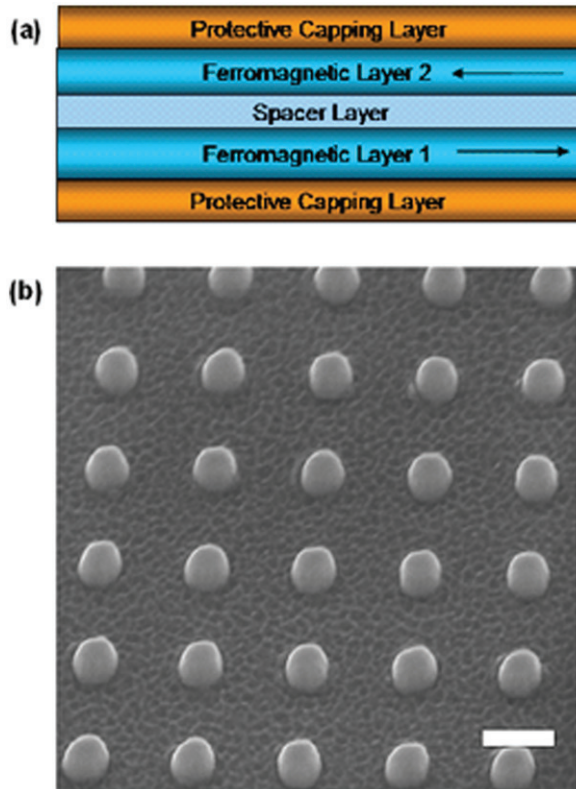


Figure 1. (Color online). (a) Schematic representation of an SAF nanoparticle structure. The arrows in the two ferromagnetic layers represent the direction of magnetization at zero applied magnetic field. (b) SEM image of an array of templated SAF nanoparticles on a Si substrate. Scale bar = 200 nm.

## 2. Experimental

### 2.1. Physical fabrication of nanoparticles

The physical fabrication of the nanoparticles has been described in detail in [13] and is only summarized in this section. Briefly, a (100) silicon (Si) wafer was sputter-coated with a 50-nm chemically etchable release layer of copper (Cu) (hereafter termed ‘release layer’). A layer of Ta (‘buffer layer’) of approximately 3 nm was then deposited to minimize oxidation of the Cu during subsequent resist bakes. Substrate-bound SAF nanoparticles were then fabricated using nanoimprinted bilayer resist templates and sequential sputter deposition of the multilayer magnetic and non-magnetic films, followed by a lift-off process in which substrate-bound SAF nanoparticles were obtained.

Releasing the SAFs from the Si substrate involves an extra step of ion milling through the thin Ta buffer layer to expose the Cu release layer. This was carried out using an ion mill etcher (Veeco Instrument Inc., Plainview, NY, USA) operated at a base pressure of  $5 \times 10^{-7}$  Torr, processing pressure of  $1.5 \times 10^{-4}$  Torr and argon ion energy of 500 eV. Ion milling was performed for 30 s at an angle of  $90^\circ$  (i.e. normal incidence). Following this, the substrate was etched with 3 ml ammonia–cupric sulfate solution, which exploits

Cu–amine complexes to attain high selectivity towards Cu. This etch was then neutralized by the addition of a citrate buffer, which also acted as a surfactant, to stabilize the nanoparticles in solution. The released particles were collected by five cycles of centrifugation and solvent exchange, and finally re-suspended in de-ionized water.

Figure 1b is an SEM image showing arrays of substrate-bound SAF nanoparticles. They appear as ‘dots’ of approximately 100 nm in diameter and are spaced 200 nm apart. Size distribution analyses of the released SAFs were carried out using TEM. Released SAF samples were pipetted onto a TEM Cu grid coated with an ultrathin layer of carbon (Ted Pella Inc., Redding, CA, USA), and images were acquired using a Philips CM20-FEG TEM operated at 200 kV. Measurements of 200 particles show that they have a Gaussian size distribution with mean diameter of 139 nm, a median diameter of 140 nm with standard deviation of 6.8 nm (5%). These statistics affirm that the SAFs are highly monodisperse in size.

## 2.2. TEM specimen preparation

TEM cross-section specimens of SAF nanoparticles were prepared for transmission electron microscopy (TEM) characterization (Figure 2). The 3-mm diameter disks, comprising templated SAF arrays, were first produced using a table-top drill press equipped with a diamond-impregnated core drill. Each disk was then glued onto a blank Si substrate of equivalent dimensions with G1 resin and hardener, mixed in the ratio 10:1 (Gatan Inc., Pleasanton, CA, USA), with the SAF array sandwiched in the resin/hardener matrix. The disks were then mechanically thinned down at their interfaces with diamond lapping films of grit sizes 30, 15, 9, 6, 3, 1, 0.5 and 0.1  $\mu\text{m}$ , via standard grinding and

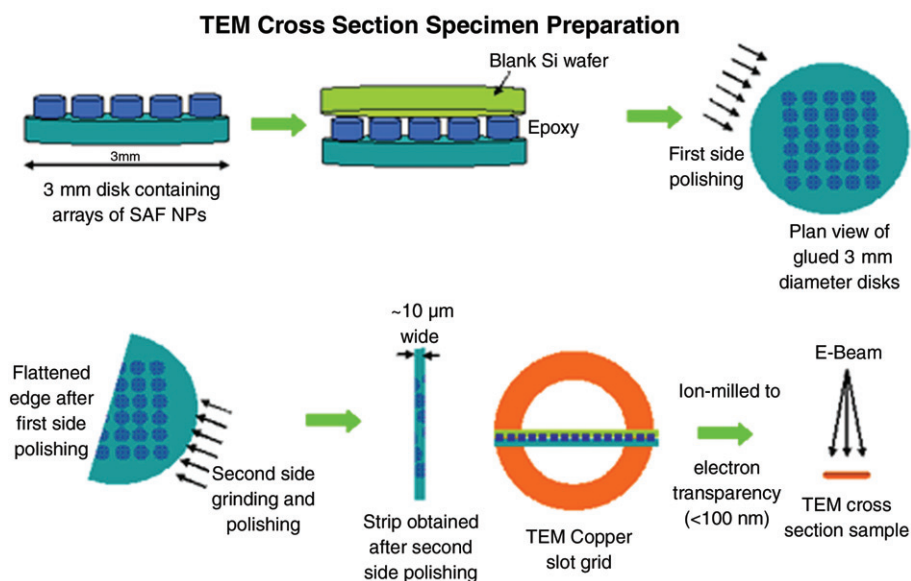


Figure 2. (Color online). Schematic diagram illustrating the TEM cross-section specimen preparation steps for substrate-bound SAF nanoparticles.

polishing tools (T-Tool, Precision TEM Inc., Santa Clara, CA, USA). During the process, the thickness of the cross-section specimen was measured using an optical microscope. Using it in transmission mode, the sample thickness was estimated based on the colour change of the Si substrate. When the sample was approximately 10  $\mu\text{m}$  thick, the Si substrate becomes light orange in colour and the specimen was removed from the T-Tool glass fixture by immersing it in acetone. It was then rotated and glued to a TEM Cu slot grid such that the interface comprising SAF nanoparticles was in the plane of the Cu grid, and further etched to electron transparency using a Gatan 691 precision ion polishing (PIPS) system.

Released SAF nanoparticles suspended in water were also prepared for TEM analyses by pipetting 5  $\mu\text{l}$  of released SAF sample onto a TEM Cu grid coated with an ultrathin layer of carbon (Ted Pella Inc., Redding, CA, USA).

All specimens were studied at the Stanford Nanocharacterization Laboratory (SNL) using a Philips CM20-FEG TEM fitted with an energy dispersive X-ray (EDS) spectrometer operating at 200 kV.

### 2.3. Specimen preparation for magnetic characterization

The magnetic hysteresis loops of substrate-bound and released nanoparticles harvested in water were measured by alternating gradient magnetometry (AGM) (MicroMag 2900, Princeton Measurements Corp., Princeton, NJ, USA). For substrate-bound SAF nanoparticles,  $3 \times 3 \text{ mm}^2$  nanoparticle arrays were used for magnetic hysteresis measurements. To further elucidate the characteristics of suspended SAF nanoparticles, samples were obtained by enclosing 10  $\mu\text{l}$  of samples in paraffin containers. This yielded approximately  $10^8$  particles, since each batch of  $10^9$  particles are suspended in 100  $\mu\text{l}$  of water.

## 3. Results and discussion

### 3.1. Characterization of multilayer-structured nanoparticles

To confirm that nanoparticles with multilayer structure can be produced, templated arrays of SAF nanoparticles were initially fabricated without the introduction of the Cu release layer. Figure 3a shows a TEM cross-section image of an array of SAF nanoparticles of target structure Si(sub)/Ta70/Ru20/Co<sub>90</sub>Fe<sub>10</sub>120/Ru25/Co<sub>90</sub>Fe<sub>10</sub>120/Ru30/Ta100, where the numbers denote nominal thicknesses in  $\text{\AA}$  units. The corresponding selected area diffraction (SAD) pattern is given in Figure 3b, which was collected from the three SAF nanoparticles shown in Figure 3a. The diameter of the SAD aperture with respect to the object plane was about 1  $\mu\text{m}$ . The specimen was oriented such that the electron beam was parallel to the [011] direction of the Si single crystal substrate. The single spot pattern is from the latter and the partial ring patterns are from the deposited films. Partial rings arise because the diffracted volume from the three SAFs (as indicated in Figure 3a) is small and so there are insufficient grains to diffract in all directions. As the diffraction spots are clustered near the 200 (kinematically forbidden) reflection of Si, for which (200) is the substrate plane, it is possible that the SAF thin films are textured. The ring patterns reveal that the films are polycrystalline in nature. The TEM camera length was calibrated using the 200 and 400 diffraction spots from the Si single crystal, and the measured interplanar

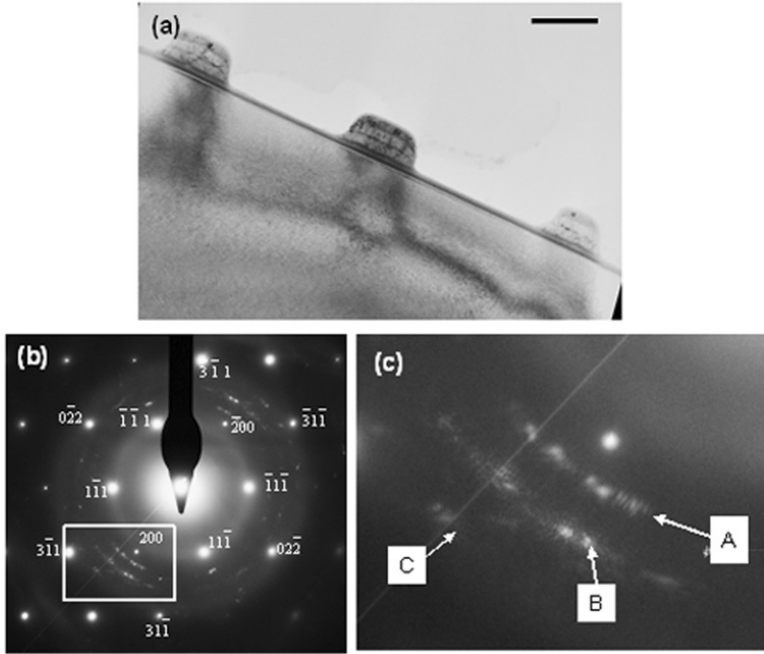


Figure 3. (a) TEM BF cross-section image of an array of SAF nanoparticles, with the scale bar denoting 100 nm. (b) Corresponding selected area diffraction (SAD) pattern. The spot patterns correspond to the  $[011]$  Si single crystal zone axis and the partial ring diffraction patterns are from the SAF nanoparticles. The  $(200)$  Si spots arise from double diffraction. The streak is due to artifacts from the TEM. (c) Magnified view of the boxed region showing the diffraction contributions from the SAFs in greater detail.

spacings were compared against powder diffraction data (JCPDS) files. Table 1 gives the interplanar spacing from partial diffraction rings A to C in Figure 3c, together with their likely material and phase of origin. Because the 200 and 400 Si spots are relatively weak, the accuracy of the camera constant is thought to be a little better than  $\pm 0.5\%$ , yielding reasonable uncertainties to the experimental  $d$ -spacings. As ring A seems to have a range of  $d$ -spacings, we also carried out the statistical evaluation of the diffraction spots to investigate the real uncertainty. The combined uncertainty of measurements, based on the camera length constant and the range of  $d$ -spacings from ring A, was found to be better than  $\pm 1\%$ .

Figure 4 shows a TEM bright-field (BF) image of a single SAF nanoparticle taken at relatively low magnification, where the multilayer structure is clearly seen. The contrast exhibited by the multilayers in this image follows those of the atomic numbers of the layers deposited:  $Z = 14(\text{Si})$ ,  $73(\text{Ta})$ ,  $44(\text{Ru})$ ,  $27(\text{Co}_{90}\text{Fe}_{10})$ ; the higher atomic number corresponding to darker layers. The constituents of each layer were verified using Nanoprobe EDS with an electron probe size of approximately 3 nm. The thicknesses of the deposited layers (averaged from eight particles) were measured as Si(sub)/Ta75/Ru31/Co<sub>90</sub>Fe<sub>10</sub>128/Ru32/Co<sub>90</sub>Fe<sub>10</sub>129/Ru33/Ta114 (numbers in Å units), reasonably close to the nominal values. There is a region of lighter contrast adjacent to the topmost Ta layer, possibly due to oxidation of the latter. Diffraction contrast from the grain structure is also evident.

Table 1. Interplanar spacing and corresponding material and phase.

Ring	Measured interplanar spacing (Å)	Corresponding interplanar spacing of material and phase	Measurement error (Å)
A	2.37	202 of $\beta$ -Ta (2.354 Å) (tetragonal) 100 of Ru (2.343 Å) (hexagonal)	$\pm 0.02$
B	2.05	111 of $\text{Co}_{90}\text{Fe}_{10}$ (2.048 Å) (fcc)	$\pm 0.01$
C	1.78	200 of $\text{Co}_{90}\text{Fe}_{10}$ (1.774 Å) (fcc)	$\pm 0.01$

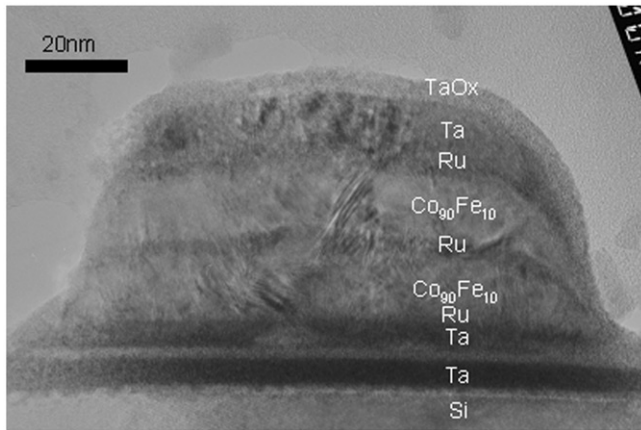


Figure 4. TEM BF image of an individual SAF nanoparticle of structure: Si(sub)/Ta70/Ru20/ $\text{Co}_{90}\text{Fe}_{10}$ 120/Ru25/ $\text{Co}_{90}\text{Fe}_{10}$ 120/Ru30/Ta100, where the numbers denote nominal thicknesses in Å units.

Figure 5 shows the magnetic hysteresis loops of the substrate-bound SAF nanoparticles. Without an external magnetic field, the remanence of these nanoparticles is nearly zero, which indicates that the magnetizations in the two  $\text{Co}_{90}\text{Fe}_{10}$  layers are anti-parallel and, thus, cancel each other as expected from considerations of magnetostatic interactions, with like poles repelling [11]. As an external field is gradually applied in the in-plane direction, this anti-parallel configuration is overcome and the magnetization starts to rotate towards the field orientation, resulting in a nearly linear increase of the net magnetization. The magnetic hysteresis curve does not show dependence on the in-plane direction of the applied field because the shape of the SAF nanoparticles is isotropic in the in-plane direction. The two magnetizations are finally parallel to each other and, thus, the particles reach magnetic saturation. The saturation magnetization value for the SAF nanoparticles is 850 emu/cc. This value is twice as large as one would achieve from magnetite ( $\text{Fe}_3\text{O}_4$ ) nanoparticles [24]. In comparison, the saturation magnetization value of bulk  $\text{Co}_{90}\text{Fe}_{10}$  is 1600 emu/cc [25]. SAFs have a lower saturation magnetization per unit volume compared to the latter because they contain non-magnetic (Ru, Ta) materials.

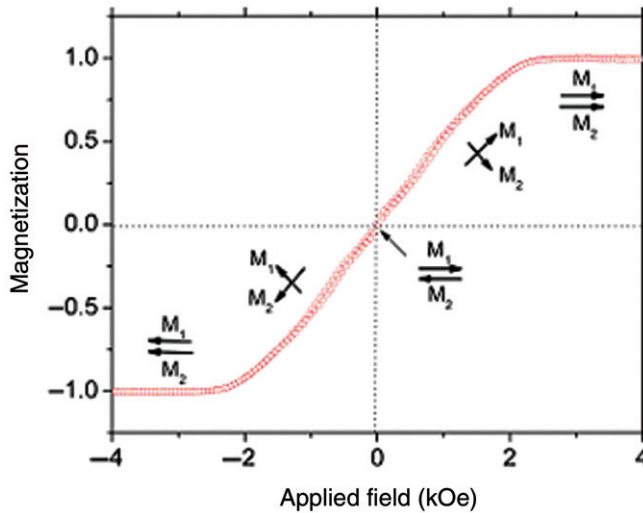


Figure 5. In-plane magnetic hysteresis measurements of substrate-bound SAF nanoparticles. The arrows schematically indicate the orientations of the magnetizations in the two CoFe magnetic layers relative to the external field.

### 3.2. SAF nanoparticles (templated and dispersed in water) fabricated using copper release layer

After verifying that multilayer-structured nanoparticles could be fabricated using nanoimprint lithography and direct deposition of layers, the next step was to construct SAF nanoparticles that could be released from the Si substrate and suspended in an aqueous medium (water). This involved the deposition of an additional chemical etchable Cu release layer and Ta buffer layer prior to subsequent deposition of the multilayer structure. As described in Section 2, the templated SAF array thus produced had to be ion milled to remove part of the Ta buffer layer to expose the Cu release layer for subsequent etching.

To examine possible differences in the structural and magnetic properties as a result of the additional layers and ion milling, SAF nanoparticles with structure Si(sub)/Ta20/Cu500(release)/Ta70(buffer)/Ru22/Co<sub>90</sub>Fe<sub>10</sub>120/Ru25/Co<sub>90</sub>Fe<sub>10</sub>120/Ru24/Ta170 were produced (numbers are nominal thicknesses in Å units). Thereafter, the substrate was cleaved into two sections. One was retained in the current state and the other was ion-milled to compare the differences in particle morphology after the ion milling process. Figures 6a and b show TEM cross-sectional images of the SAF arrays before and after the ion milling, respectively. The shape of the SAFs is transformed from cylindrical to one that is more dome-like after ion milling. In Figure 6a, the presence of the Ta buffer layer above the Cu release layer before the ion milling process is clearly visible. After ion milling (Figure 6b), the entire Ta buffer layer and part of the Cu release layer are removed, exposing the Cu surface for the subsequent chemical etch process. By analyzing higher-magnification TEM images of the before- and after-ion-mill samples, we estimated that approximately 70 Å of Ta was removed during ion milling. There is apparently little or no effect on the multilayer structure, as would be expected from such mild ion-milling conditions.

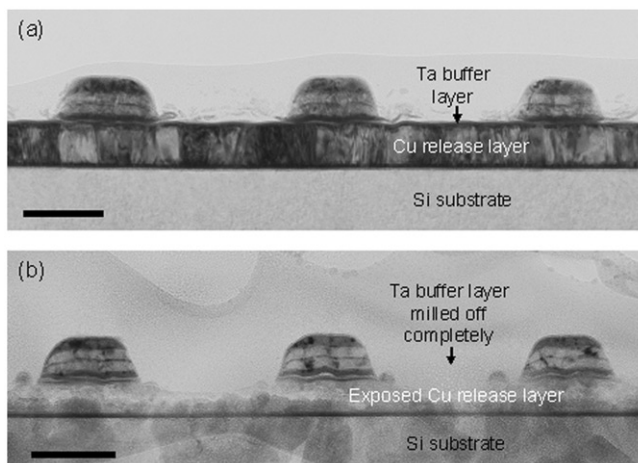


Figure 6. TEM cross-section images of SAF arrays (a) before and (b) after ion milling. In (a), the Ta buffer layer and Cu release layer are present in the before-ion-mill specimen. (b) After ion milling, the Ta buffer layer is completely removed and part of the Cu release layer is exposed for subsequent chemical etching to release the particles from substrate. The structure is Si(sub)/Ta20/Cu500(release)/Ta70/Ru22/Co<sub>90</sub>Fe<sub>10</sub>120/Ru25/Co<sub>90</sub>Fe<sub>10</sub>120/Ru24/Ta170 before ion milling, and Si(sub)/Ta20/Cu500/Ta70/Ru22/Co<sub>90</sub>Fe<sub>10</sub>120/Ru25/Co<sub>90</sub>Fe<sub>10</sub>120/Ru24/Ta100 after ion milling, where the numbers are nominal thicknesses in Å units. The scale bars in both images denote 100 nm.

Figure 7a shows a TEM BF image of an after-ion-mill SAF nanoparticle taken at higher magnification. There is a strongly diffracting Cu grain (marked X) in the release layer whose composition is verified using EDS (Figure 7b) with an electron probe size of ~5 nm. From Figure 6b, it can be observed that the multilayers are ‘wavy’ with undulations of the upper layers conforming to those of the previously deposited layers. The waviness of the layers appears to be due to the propagation of the rough Cu grains in the release layer.

The final fabrication process involved etching away the Cu release layer and harvesting the SAF nanoparticles in water. Figure 8a shows a TEM BF image of an SAF nanoparticle from the same imprint after the release process. The resolution of this image is not as good as previous cross-section TEM images due to chromatic aberrations from the increased specimen thickness (>100 nm), but one can still observe that the layered nature of the SAFs is preserved after the chemical-etching process (also see Figure 1f in [13]). The wavy nature of the layers is also evident in Figure 8a due to direct manifestation of the earlier fabrication steps.

The magnetic properties of the SAFs and their changes before ion mill, after ion mill and after release are indicated in Figure 8b. The superposition of the magnetic hysteresis loops before and after ion mill indicates a slight decrease in the magnetic moments after the ion-milling process. This might be attributed to reduced Ta passivation on the side walls of the nanoparticles after ion milling, leading to some oxidation of the ferromagnetic constituents.

Released SAFs (in water) typically show a reduction of the saturation field, as indicated in Figure 8b. This may be due to increased inter-particle interactions between the

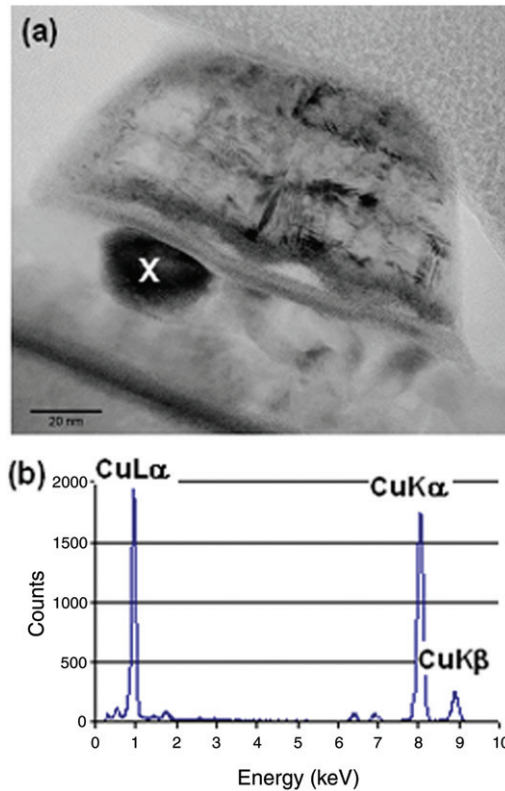


Figure 7. (Color online). (a) SAF nanoparticle with structure Si(sub)/Ta20/Cu500/Ta70/Ru22/CoFe120/Ru25/CoFe120/Ru24/Ta100 (numbers in Å) and (b) nanoprobe EDS Spectrum of copper grain (X).

magnetized nanoparticles. The reduction of the saturation field is unlikely to be related to the arbitrary direction of applied field in the liquid with respect to the structure of the MNPs as opposed to the substrate-bound MNPs. This is because a hypothetical arbitrariness in direction would have the magnetic field partially out of the particle plane, so that the magnetic field component perpendicular to the particle plane will be ineffective (high demagnetizing fields) in magnetizing the particle. In this case, the saturation field would be expected to increase. This effect was not observed in our measurements. Moreover,  $MH/kT \gg 1$  ( $M$  being the magnetization and  $H$  the applied field), which implies that particles are highly aligned by the magnetic field when they are free to rotate in solution. Deliberate tilting of the substrate plane (for anchored particles) relative to the applied field does increase the apparent saturation field. From our measurements, the ratio of remanent magnetization to saturation magnetization ( $M_r/M_s$ ) of the released SAFs is usually less than 0.02. Since  $M_s$  of SAFs is 850 emu/cc, the remanent magnetization per unit volume does not exceed 17 emu/cc.

The shapes of the magnetic hysteresis loops can be attributed to the spin flop and negative remanence phenomena [20,26,27], which leads to a slightly flatter region in the middle of the hysteresis loop. It arises from magnetic anisotropies (easy axes) in the individual ferromagnetic layers. Basically, one expects a linear slope for  $M$  versus  $H$  from

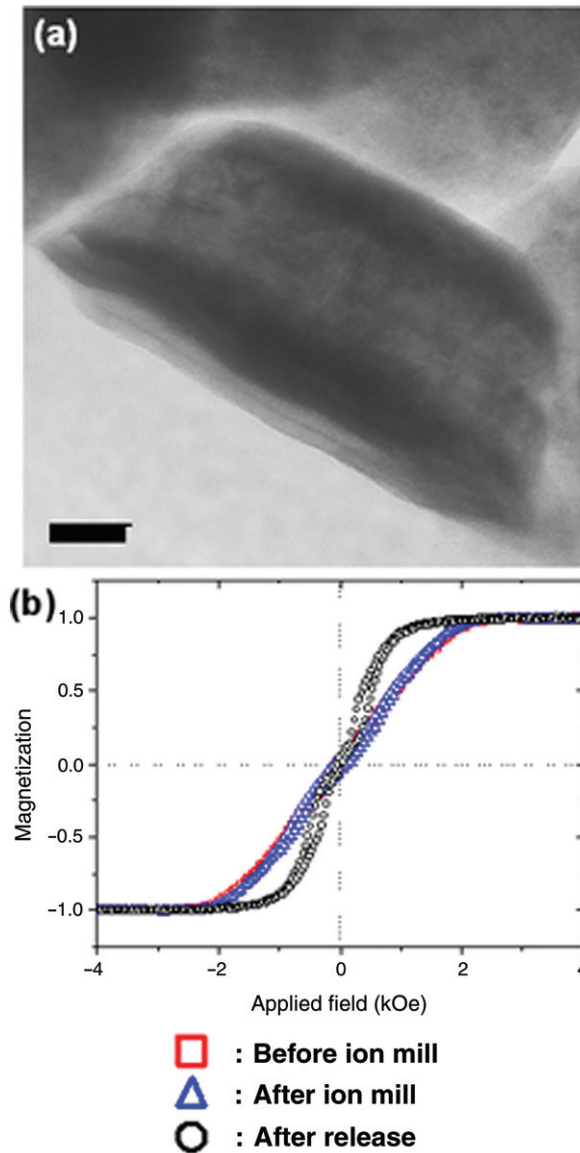


Figure 8. (Color online). (a) TEM BF image of a released SAF nanoparticle on an ultrathin carbon grid showing the layered nature of the particles. Scale bar = 20 nm. (b) Magnetic hysteresis loops of substrate-bound SAF nanoparticles before ion mill (red), after ion mill (blue) and after release in aqueous solution (black). The hysteresis loops of the SAF nanoparticles in solution indicate that there is a reduction of saturation field.

the demagnetizing field and the Ru-mediated interlayer interactions. With increasing  $H$  (before saturation), the moments are nearly anti-parallel, but both rotate (staying antiparallel) from the easy to the hard axes of the magnetically induced uniaxial anisotropies as the field is increased. The cause of such anisotropies is still

under investigation. In addition, the hysteresis loop of the released SAFs ‘opens’. One possible explanation is that magnetization of the particles in solution may cause them to experience non-coherent rotation and form chains. This effect is also under current investigation. The suspended SAF nanoparticles still retain low magnetic remanence when the external field is removed.

From our experience, the ion-milling step can be destructive and can lead to severe degradation of the particles if the conditions are not monitored carefully. Figure 9 shows a TEM BF image of a released SAF nanoparticle (from a different batch) from a substrate which has been ion-milled for 35 s instead of the usual 30 s. The increase in ion-milling time led to part of the ferromagnetic layer being exposed. The utility of TEM examination is also demonstrated by such observations.

### 3.3. Comparison of SAF nanoparticles fabricated on different release layers and with varying ferromagnetic layer thicknesses

To investigate the effects of different release layers and ferromagnetic thicknesses on the SAFs’ structural and magnetic properties, samples of Si/Ta30/[Layer]500/Ta70/Ru20/Co<sub>90</sub>Fe<sub>10</sub>[*t*]/Ru25/Co<sub>90</sub>Fe<sub>10</sub>[*t*]/Ru20/Ta70 were fabricated, where [Layer] denotes either a (i) Cu release layer of nominal thickness 500 Å (‘Cu release layer’), or (ii) Cu release layer of nominal thickness 500 Å with the introduction of  $1.3 \times 10^{-5}$  Torr of oxygen during its deposition using a variable leak valve (hereafter termed ‘CuOx release layer’). The introduction of oxygen came about after it was reported in the literature that the island growth of Cu could be suppressed with the addition of oxygen [28], producing flatter layering. For the two types of release layers, the thickness of the ferromagnetic Co<sub>90</sub>Fe<sub>10</sub> layer was also varied by setting [*t*] as 60 or 120 Å (with equal ferromagnetic layer

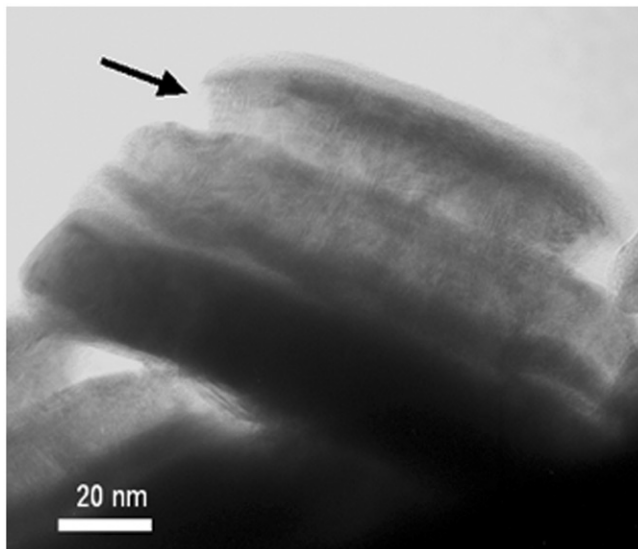


Figure 9. TEM BF image of a defective SAF nanoparticle whose ferromagnetic layer had been partially removed due to over ion-milling.

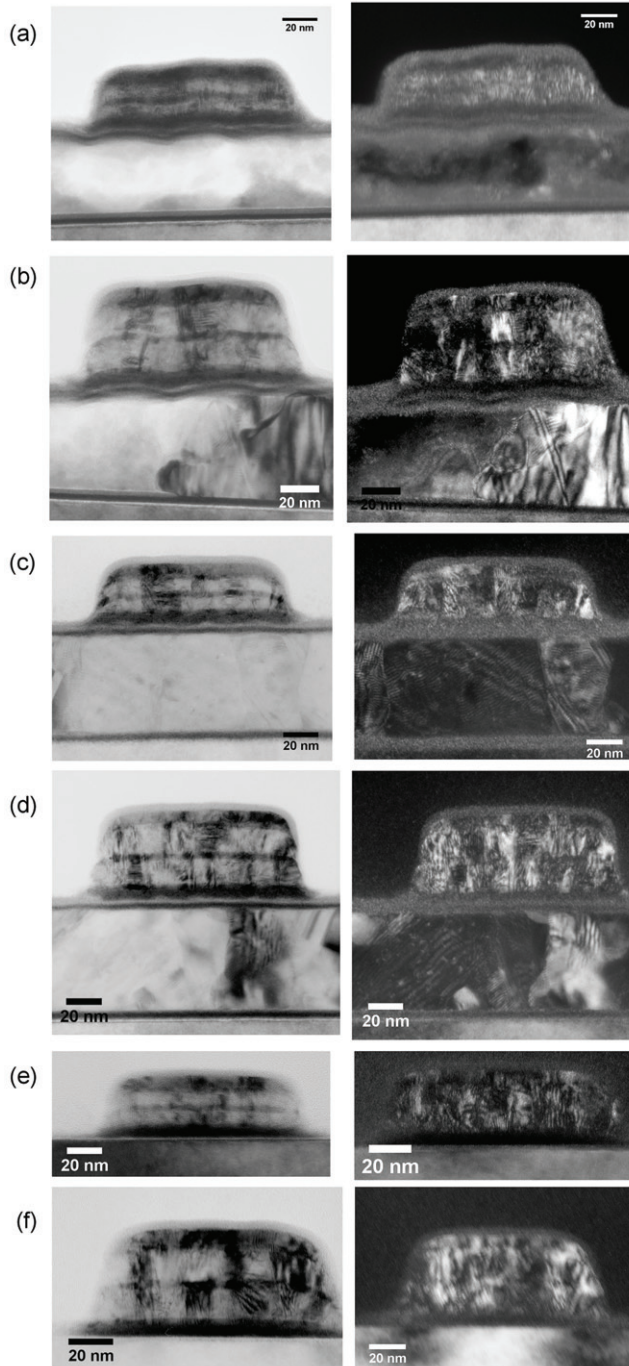


Figure 10. TEM BF (left panel) and CDF (right panel) pairs of SAFs of structure Si/Ta30/[Layer]500/Ta70/Ru20/Co<sub>90</sub>Fe<sub>10</sub>[*t*]/Ru25/Co<sub>90</sub>Fe<sub>10</sub>[*t*]/Ru20/Ta70, where [Layer] denotes the material of the release layer and [*t*] denotes the thickness of the Co<sub>90</sub>Fe<sub>10</sub> ferromagnetic layer in Å units. In (a) and (b), [Layer] = copper release layer and [*t*] = 60 and 120 Å, respectively. In (c) and (d), [Layer] = copper oxide release layer and [*t*] = 60 and 120 Å, respectively. (e) and (f) Control samples of SAFs fabricated on Si substrate (without release layer) and have structure Si/Ta40/Ru20/Co<sub>90</sub>Fe<sub>10</sub>[*t*]/Ru25/Co<sub>90</sub>Fe<sub>10</sub>[*t*]/Ru20/Ta70, where [*t*] = 60 Å in (e) and 120 Å in (f). Numbers denote nominal thicknesses in Å units.

thicknesses in an individual sample). In addition, control samples of Si/Ta40/Ru20/Co<sub>90</sub>Fe<sub>10</sub>[*t*]/Ru25/Co<sub>90</sub>Fe<sub>10</sub>[*t*]/Ru20/Ta70 (i.e. without any release layer), where [*t*] = 60 or 120 Å, were also fabricated, making a total of six samples.

To examine possible differences in SAF structures from the various configurations, TEM BF and complementary centred dark-field (CDF) images were acquired from each of the six samples and are illustrated in Figure 10. CDF imaging involves tilting the beam so that the diffracted beam is parallel to the TEM optic axis [29]. An objective aperture is used to select the diffracted beam. Grains that strongly diffract into this diffracted beam appear bright in the CDF images. SAFs, whose structure are deposited on the Cu release layer, have wavy topography, consistent with our previous observations. In comparison, SAFs on CuOx have layers that are straighter and are comparable to the control samples that do not have any release layer. From the CDF images, the grains in each layer of SAF nanoparticles fabricated on CuOx release layer have more parallel grain orientations, as indicated by the strong diffraction of the latter throughout the particles.

From lower magnification TEM BF and CDF images, we noted the presence of columnar grain formation in the Cu release layer (Figure 11a). This effect was suppressed in the CuOx release layer (Figure 11b). The differences in grain structure in the two release layers were also confirmed from their respective SAD patterns (Figure 11a and b, insets). Grains in the Cu release layer appear to have a strong  $\langle 111 \rangle$  texture (arrows in Figure 11a inset), whereas the CuOx grains appear to be more randomly oriented (box in Figure 11b inset). In both cases, the samples were oriented so that the electron beam was parallel to the [011] direction of the Si single crystal substrate. The SAD aperture was used to select the Si substrate and release layers. Of course, we also evaluated the uncertainty of the measured interplanar spacing of Cu and found it to be within 0.5% of the expected value, based on the camera length constant calibrated from measuring the interplanar spacings of the 200 and 400 diffraction spots from the Si single crystal, consistent with our previous analysis (Table 1).

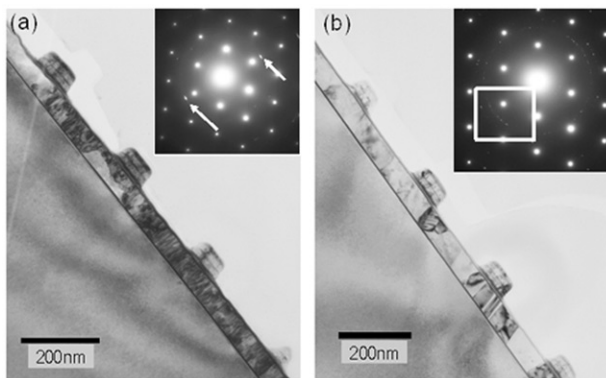


Figure 11. (a) Low magnification TEM CDF image of SAFs on copper release layer with SAD pattern inset, revealing the strong [111] texture of copper grains. (b) Low magnification TEM BF image of SAFs on oxidized copper release layer, where the SAD pattern (inset) shows that the grains are more randomly oriented. The Si substrate is oriented in the [011] direction in both cases.

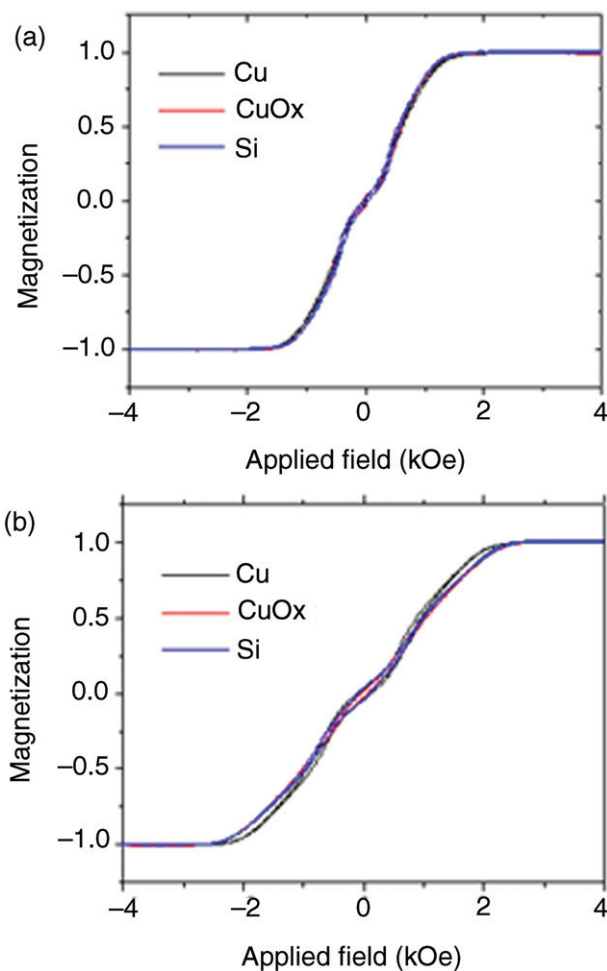


Figure 12. (Color online). AGM measurements of SAFs with structure Si/Ta30/[Layer]500/Ta70/Ru20/Co<sub>90</sub>Fe<sub>10</sub>[*t*]/Ru25/Co<sub>90</sub>Fe<sub>10</sub>[*t*]/Ru20/Ta70, where [Layer] = Cu release layer or CuOx release layer and [*t*] = 60 or 120 Å. Control samples of SAFs fabricated on Si substrate (without release layer) have structure Si/Ta40/Ru20/Co<sub>90</sub>Fe<sub>10</sub>[*t*]/Ru25/Co<sub>90</sub>Fe<sub>10</sub>[*t*]/Ru20/Ta70, where [*t*] = 60 or 120 Å. Numbers denote nominal thicknesses in Å units.

Despite an improvement in morphology, the influence on magnetic properties is not dramatic. Figure 12 shows the magnetic characterization data for SAF nanoparticles with different release layers. The shapes of the hysteresis loops are similar to those observed in Figure 8b, which we attribute to the spin flop and negative remanence effects [20,26,27]. The changes in  $M-H$  loops for the different samples are insignificant. One of the reasons is that the Ru spacer layer in the SAF structure (at 2.5 nm) is thick, so that interlayer exchange coupling is too weak to be effective. Reducing Ru spacer layer thickness to a certain range (such as  $<7 \text{ \AA}$ ) is expected to result in stronger antiferromagnetic exchange coupling [30,31], but the saturation field of such SAF nanoparticles is too large to be useful for the applications in which we are currently interested.

The thickness of the ferromagnetic layers has a direct effect on the external magnetic field required for the particles to attain saturation magnetization. When the ferromagnetic layer thickness is doubled from 60 to 120 Å, this saturation field increases from 1.3 to 2.1 kOe, but again appears to be independent of the release layer. The saturation magnetization of the particles per unit volume doubles from 425 to 850 emu/cc with doubling of the ferromagnetic layer thicknesses due to the two-fold increase in volume of its magnetic constituents. There is no apparent difference in the structure between the two thicknesses of the  $\text{Co}_{90}\text{Fe}_{10}$  layers.

#### 4. Conclusions

In summary, SAF nanoparticles composed of multilayer thin films have been fabricated. Unlike other MNPs synthesized via conventional chemical routes, their morphologies have been pre-determined from the initial fabrication process. Magnetic measurements show that these nanoparticles have nearly zero magnetic remanence and coercivity, and linear response of magnetization. The use of ferromagnetic materials has enabled the SAFs to achieve higher saturation magnetizations than their chemically synthesized iron oxide counterparts. Our analyses from TEM cross-section specimens show that these nanoparticles possess characteristics similar to those of sputtered magnetic multilayer thin films. TEM micrographs of the released particles indicate that the layered structure is preserved after the chemical etch, and that they are highly monodisperse in terms of size. From magnetic measurements, there was a slight decrease in magnetic moment of the SAFs after ion milling, which we attributed to oxidation of the ferromagnetic constituents due to reduced Ta passivation on the side walls of the SAFs. A key finding from our study is the improvement in topography of the SAF layers, through the introduction of a small amount of oxygen during deposition of the copper release layer, as shown by cross-section TEM. The unique fabrication method and structure of the SAF nanoparticles make them interesting candidates for further study, with a view to possible applications in cancer detection.

#### Acknowledgements

This project is supported by the Stanford University Center for Cancer Nanotechnology Excellence Focused on Therapy Response (CCNE-TR) grant (NIH U54) and the Nanyang Technological University (Singapore) Overseas Scholarship (ALK).

#### References

- [1] Q.A. Pankhurst, J. Connolly, S.K. Jones et al., *J. Phys. D: Appl. Phys.* 36 (2003) p.R167.
- [2] A.K. Gupta and M. Gupta, *Biomaterials* 26 (2005) p.3995.
- [3] P. Tartaj, M. del Puerto Morales, S. Veintemillas-Verdaguer et al., *J. Phys. D: Appl. Phys.* 36 (2003) p.R182.
- [4] D.K. Kim, Y. Zhang, W. Voit et al., *Scripta Mater.* 44 (2001) p.1713.
- [5] T. Neuberger, B. Schöpf, H. Hofmann et al., *J. Magn. Magn. Mater.* 293 (2005) p.483.
- [6] U. Häfeli, W. Schütt, J. Teller et al., (Editors), *Scientific and Clinical Applications of Magnetic Carriers*, Plenum Press, New York, 1996.

- [7] C. Xu and S. Sun, *Polym. Int.* 56 (2007) p.821.
- [8] T. Hyeon, *Chem. Commun* (2003) p.927. doi: 10.1039/b207789b.
- [9] J. Park, K. An, Y. Hwang et al., *Nat. Mater.* 3 (2004) p.891.
- [10] A.L. Koh and R. Sinclair, in *Technical Proceedings of the 2007 Nanotechnology Conference and Trade Show 4* (CRC Press, Boca Raton, FL 2007), p.101.
- [11] B.D. Cullity, *Introduction to Magnetic Materials*, Addison-Wesley, Reading, MA, 1972.
- [12] R.J. Wilson, US Patent 5932097 (1999, 2002).
- [13] W. Hu, R.J. Wilson, A.L. Koh et al., *Adv. Mater* 20 (2008) p.1479.
- [14] S.Y. Chou, P.R. Krauss and P.J. Renstrom, *Science* 272 (1996) p.85.
- [15] B. Heidari, I. Maximov, E. Sarwe et al., *J. Vac. Sci. Tech. B* 17 (1999) p.2961.
- [16] W. Hu, R.J. Wilson, L. Xu et al., *J. Vac. Sci. Tech. A* 25 (2007) p.4.
- [17] S.X. Wang, R.J. Wilson and W. Hu, US Provisional Patent Application No. 60/760, 221 (2006).
- [18] A.L. Koh, W. Hu, R.J. Wilson et al., *Microsc. Microanal.* 13 (Suppl. 2) (2007) p.66CD.
- [19] K. Inomata, T. Nozaki, N. Tezuka et al., *Appl. Phys. Lett.* 81 (2002) p.310.
- [20] S.C. Byeon, A. Misra, P.B. Visscher et al., *IEEE Trans. Magn.* 40 (2004) p.2359.
- [21] H.C. Tong, C. Qian, L. Miloslavsky et al., *J. Appl. Phys.* 87 (2000) p.5055.
- [22] Y. Huai, J. Zhang, G.W. Anderson et al., *J. Appl. Phys.* 85 (1999) p.5528.
- [23] A. Veloso and P.P. Freitas, *J. Appl. Phys.* 87 (2000) p.5744.
- [24] R.C. O'Handley, *Modern Magnetic Materials: Principles and Applications*, Wiley, New York, 2000, p.99.
- [25] T. Hikosaka, US Patent 6548194 (2003).
- [26] P.J.H. Boemen, H.W. van Kesteren, H.J.M. Swagten et al., *Phys. Rev. B* 50 (1994) p.13505.
- [27] B. Dieny and J.P. Gavigan, *J. Phys. Condens. Matter* 2 (1989) p.187.
- [28] H. Li, Y. Wu, J. Qiu et al., *Appl. Phys. Lett.* 79 (2000) p.3663.
- [29] D.B. Williams and C.B. Carter, *Transmission Electron Microscopy: A Textbook for Materials Science*, Plenum Press, New York, 1996, p.143.
- [30] S.S.P. Parkin, N. More and K.P. Roche, *Phys. Rev. Lett.* 64 (1990) p.2304.
- [31] S.S.P. Parkin, *Phys. Rev. Lett.* 67 (1991) p.3598.